Analysis of the wavelength-to-depth encoded interference microscopy for three-dimensional imaging

Guoqiang Li, MEMBER SPIE
Yeshayahu Fainman, MEMBER SPIE
University of California, San Diego
Department of Electrical and Computer Engineering
La Jolla, California 92093-0407
E-mail: guoqli@hotmail.com

Abstract. An interference microscope based on a wavelength-to-depth encoding technique is analyzed. The wavelength-to-depth encoding is achieved with a diffractive lens and a wavelength-tunable laser. The theoretical depth resolution is consistent with the experimental result. The technique offers a comparable depth resolution as traditional depth scanning. With the rapid advances in microfabrication and wavelength-tunable lasers, the system is promising for fast, noncontact, and high-resolution three-dimensional imaging. [DOI: 10.1117/1.1474439]

Subject terms: interference microscopy; Fourier optics; coherence; three-dimensional imaging.

Paper 010231 received July 2, 2001; revised manuscript received Dec. 28, 2001; accepted for publication Jan. 3, 2002.

1 Introduction

High-resolution noncontact three-dimensional imaging techniques are very attractive for many applications. Various methods for 3-D profilometry based on optical interferometry have evolved, including confocal imaging techniques[1–4] and interference microscopy.[5–12] Interference microscopy can eliminate lateral scanning. In this scheme, the depth information is obtained by measuring the degree of coherence rather than the phase between corresponding pixels in the object and reference planes. It uses the entire available illumination, and all the transverse points are measured in parallel. It is capable of the same transverse resolution and depth response as a confocal microscope. As a result, different types of architecture based on the Linnik microscope,[5] the Mirau correlation microscope,[6,7] and the Michelson interferometer[8–12] have been proposed. In these systems, the object is scanned along the vertical axis (z axis) by a piezoelectric translation stage. To avoid mechanical depth scanning, recently we applied a wavelength-to-depth encoding technique to a Linnik-type interferometric microscope for 3-D imaging.[13] It achieves longitudinal scanning by focusing the light of different wavelengths onto different planes of the object. Depth encoding is realized by a diffractive lens combined with wavelength tuning. This construction results in a novel interferometric microscope architecture, where diffractive and refractive imaging systems are used in the object arm and reference arm, respectively. Experimental results have been reported in Ref. 13. We focus on analysis of the coherence property of the optical fields from both arms with the change of wavelength. The experimental value of depth resolution is consistent with the theoretical analysis.

2 Interference Microscope System with Wavelength-to-Depth Encoded Scanning

A schematic diagram of our interference microscope setup is shown in Fig. 1. The linearly polarized quasimonochromatic light from a wavelength-tunable Ti:sapphire laser is used in our experiments. The collimated beam is transmitted through a rotating ground glass, which generates a spatially incoherent optical field to be used in the interference microscope. The interference microscope has an object arm and a reference arm each with a 4-f imaging system.

The coherence characteristic of a spatially incoherent source can be described by the mutual intensity function,[14] which can be calculated by means of the Van Cittert-Zernike theorem. According to this theorem, the coherence area is defined such that the light from any two points within the coherence area will interfere. This also implies that light from two different coherence areas will be incoherent. For free space propagation, the size of the coherence area is proportional to the distance between the observation plane and the ground glass, and it is inversely proportional to the size of the light source. Therefore the optical field in the observation plane can be divided into small elementary cells called coherence cells, and the size of the coherence cell is related to that of the coherence area. With this approach, coherence volumes can be further defined with their height being the coherent length of the source. With reference to Fig. 1, when the spatially incoherent light is separated into two parts by the beamsplitter, two sets of coherence cells are created in the two planes equidistant from the ground glass. Any coherence cell in one plane will be coherent with one and only one coherent cell in the other plane. If the two corresponding coherence cells are overlapped, inference fringes with high contrast will be observed. The two corresponding cells are defined as a coherent cell pair.

We employ a 4-f imaging system consisting of a diffractive lens (L1) and an objective lens (L2) in the object arm to inversely image the coherent cells in the plane x_1y_1 to the object plane, with x_1y_1 being the focal plane of the diffractive lens for the center wavelength λ_c of our system.

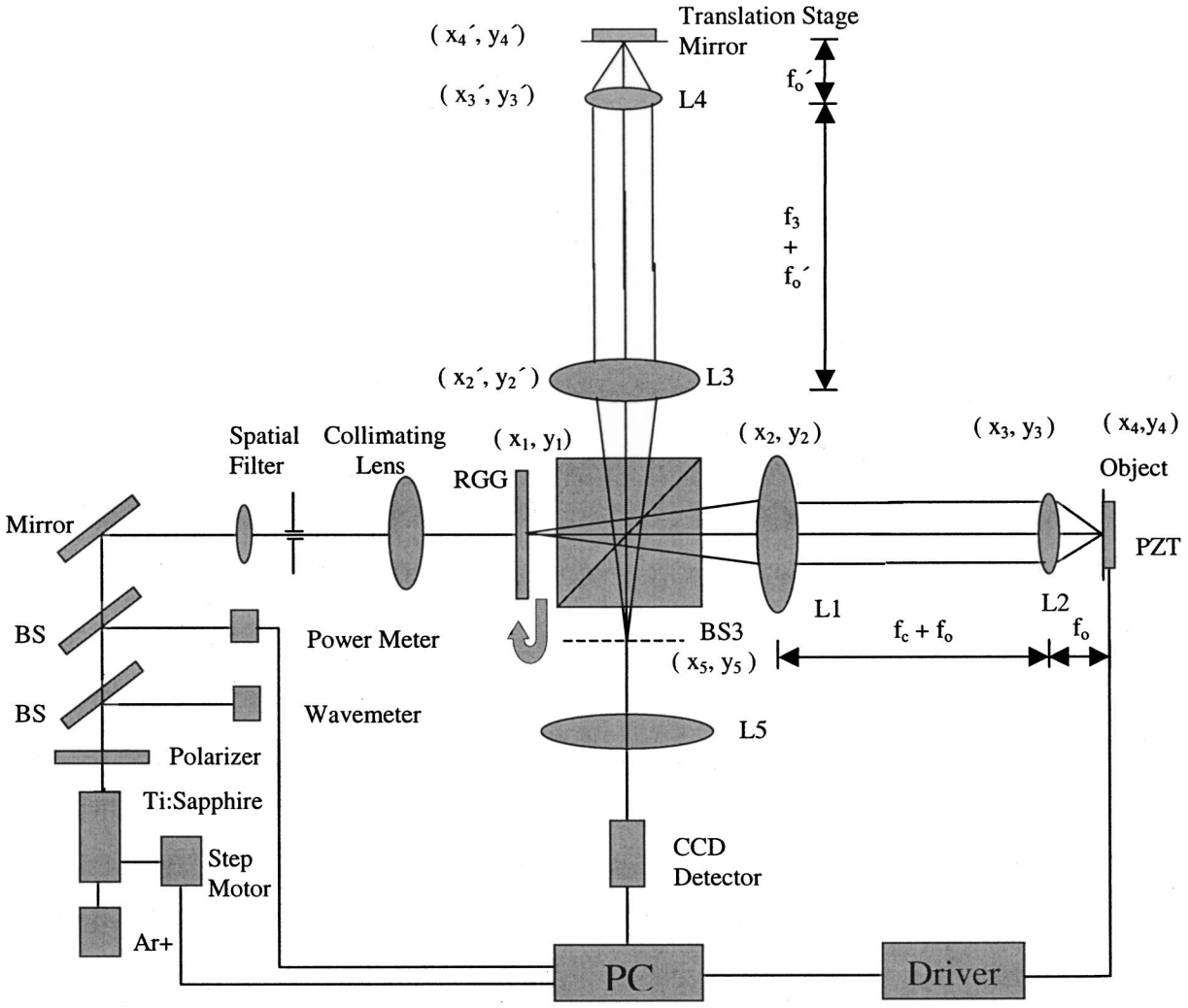

Fig. 1 Configuration of the interference microscope using wavelength-to-depth encoding. BS is the beamsplitter; and RGG is the rotating ground glass.

To compensate for the path length difference between the two arms, another 4-f imaging system consisting of a large-aperture achromatic refractive lens (L3) and an objective lens (L4) is adopted in the reference arm. The coherent cells in the object plane and the reference mirror are imaged back to the plane x_5y_5, respectively. The overlapped optical fields are imaged through the lens (L5) onto the CCD, where the interference patterns are detected and recorded.

Before presenting the coherence degree function of the system versus wavelength, we briefly discuss the imaging characteristic of the object arm. For the first-order diffraction, a linear approximation of the focal length of the diffractive lens at wavelength λ is given by[15]

$$f(\lambda)=2f(\lambda_d)-\frac{f(\lambda_d)}{\lambda_d}\lambda, \tag{1}$$

where λ_d and $f(\lambda_d)$ are the design wavelength and the corresponding focal length, respectively. Under this approximation, the focal length changes linearly with the change of the operating wavelength. The larger the wavelength, the shorter the focal length. Suppose the object arm is aligned for the center wavelength $\lambda_c=863$ nm. The corresponding focal length of the diffractive lens is f_c and the coherent cells in the plane x_1y_1 are imaged to the plane with an image distance f_o, f_o being the focal length of the objective lens. When the operating wavelength is tuned away from λ_c by $\Delta\lambda$, there will be a corresponding focal length change Δf of the diffractive lens L_1, and consequently, the coherent cells in the plane x_1y_1 will be imaged to the plane with an image distance $f_o+\Delta z$. According to the Gaussian imaging law in geometry optics, the relation between the displacement Δz and Δf takes the form

$$\Delta z=\frac{f_O^2}{f_C^2/\Delta f+2f_C}. \tag{2}$$

In terms of Eq. (1), we have

$$\Delta f(\lambda)=-\frac{f(\lambda_d)}{\lambda_d}\Delta\lambda. \tag{3}$$

If $f_C \gg \Delta f$, Eq. (2) can be approximated as

$$\Delta z = \left(\frac{f_O}{f_C}\right)^2 \Delta f = -\left(\frac{f_O}{f_C}\right)^2 \frac{f(\lambda_d)}{\lambda_d}\Delta\lambda. \quad (4)$$

This means that when the focal length increases (the operating wavelength decreases), the image distance also increases, i.e., the image plane is further from the objective lens, and vice versa. If we put a reflection mirror in the back focal plane of the objective lens, the optical field incident on the mirror will change with the change of the wavelength. Furthermore, the reflected optical field will be imaged back onto or off the plane x_5y_5, and hence the optical field incident on the plane x_5y_5 will also change with the change of the wavelength. To find the coherence function of the optical fields coming from the object and the reference arms, we need to analyze the impulse responses of the two arms at wavelength λ.

The impulse response can be analyzed by Fourier optics.[16] Assume the size of the coherence cell in plane x_1y_1 is small, so that its optical field can be approximated by a δ-function distribution. For simplicity and without the loss of generality, consider an on-axis point source first. For both the object and the reference arms, the impulse response can be obtained in two steps: 1. generate the optical field distribution $U_4(x,y)$, which is the point spread function of the first subsystem from plane x_1y_1 to plane x_4y_4; 2. The complex amplitude of the optical waves $U_5(x,y)$ in plane x_5y_5 is the ideal geometrical image of $U_4(x,y)$ convoluted by the point spread function of the second subsystem from plane x_4y_4 to plane x_5y_5. In the 4-f imaging systems, the apertures of the eyepieces (the diffractive lens L1 and the refractive lens L3) are large in comparison with the beam size, whereas the apertures of the two objective lenses have spatial limitations on the wavefronts.

In the object arm, from plane x_1y_1 to plane x_4y_4, the optical wave totally undergoes two lenses and three free space sections. The resulting wavefield from the free space propagation through a distance d can be calculated by the Fresnel diffraction:

$$U_n(x,y) = \int\int U_m(x',y')h_{mn}(x-x',y-y')dx'dy', \quad (5)$$

where $U_m(x',y')$ is the input field, $U_n(x,y)$ is the output field in the observation screen, and the convolutional kernel h_{mn} is defined as the free space propagation operator

$$h_{mn} = B_{mn}\exp\left[j\frac{k}{2d_{mn}}(x^2+y^2)\right] = B_{mn}Q(x,y,d_{mn}), \quad (6)$$

in which $B_{mn}=[\exp(jkd_{mn})/j\lambda d_{mn}]$, $k=2\pi/\lambda$, d_{mn} is the distance between the input and output planes, and $Q(x,y,d_{mn})$ is used to denote the quadratic phase function. For a thin lens transmission, the complex field $U_l^+(x,y)$ across a plane immediately behind a lens is related to the complex field $U_l^-(x,y)$ incident on a plane immediately in front of the lens by

$$U_l^+(x,y) = U_l^- \exp\left[-j\frac{k}{2f}(x^2+y^2)\right] = U_l^- Q^*(x,y,f), \quad (7)$$

where f is the focal length of the lens, and the superscript * represents a complex conjugate. Therefore, the input distribution is first operated on by a free space propagation operator through a distance f_c and the wavefield incident on the diffractive lens is given by

$$U_2^-(x,y) = B_{12}Q(x,y,fc). \quad (8)$$

The complex amplitude transmitted by the diffractive lens is then

$$U_2^+(x,y) = U_2^-(x,y)Q^*(x,y,f_\lambda). \quad (9)$$

A second free space propagation operates on $U_2^+(x,y)$ through a distance f_c+f_o and the wave field incident on the objective lens may be written as

$$U_3^-(x,y) = U_2^+(x,y)^{**}[B_{23}Q(x,y,f_c+f_o)], \quad (10)$$

where ** represents a convolution operation, and the complex amplitude leaving the objective lens becomes

$$U_3^+(x,y) = U_3^-(x,y)p(x,y)Q^*(x,y,f_o), \quad (11)$$

in which $p_1(x,y)$ is the aperture function of the objective lens. Finally, with a third free space propagation through a distance f_o, we obtain the optical field distribution in the plane x_4y_4 as

$$U_4^-(x,y) = U_3^+(x,y)^{**}[B_{34}Q(x,y,f_o)]. \quad (12)$$

Substituting Eqs. (8), (9), (10), and (11) into (12), yields the following results

$$\begin{aligned} U_4^-(x_4,y_4) &= B_{12}B_{23}B_{34}B_\lambda Q(x_4,y_4,f_o) \\ &\quad \times F\left\{p(x,y)\exp\left[jk\frac{(f_\lambda-f_c)(x^2+y^2)}{2(2f_cf_\lambda-f_c^2+f_of_\lambda-f_of_c)}\right]\right\}\Bigg|_{\xi=\frac{x_4}{\lambda f_o},\ \eta=\frac{y_4}{\lambda f_o}} \\ &= CQ(x_4,y_4,f_o) \\ &\quad \times F\left\{p(x,y)\exp\left[jk\frac{(f_\lambda-f_c)(x^2+y^2)}{2(2f_cf_\lambda-f_c^2+f_of_\lambda-f_of_c)}\right]\right\}\Bigg|_{\xi=\frac{x_4}{\lambda f_o},\ \eta=\frac{y_4}{\lambda f_o}}, \end{aligned} \quad (13)$$

where $C=B_{12}B_{23}B_{34}B_\lambda$,

$$B_\lambda = j\lambda \Big/ \left(\frac{1}{f_c}-\frac{1}{f_\lambda}+\frac{1}{f_c+f_o}\right),$$

F is the Fourier transform operator, and ξ and η are variables of spatial frequency. Actually, Eq. (13) is the point spread function $[h_1(x_4,y_4)]$ of the first subsystem. When $f_o \ll f_c$ and $(f_\lambda - f_c) \ll f_c$, Eq. (13) can be simplified as

$$h_1(x_4,y_4)=U_4^-(x_4,y_4)$$
$$=CQ(x_4,y_4,f_o)F\left\{p(x,y)\exp\left[jk\frac{(f_\lambda-f_c)}{2f_c^2}\times(x^2+y^2)\right]\right\}\Bigg|_{\xi=\frac{x_4}{\lambda f_o},\quad \eta=\frac{y_4}{\lambda f_o}}$$
$$=CQ(x_4,y_4,f_o)F\{p(x,y)\times\exp[jkW_1(x,y)]\}\Bigg|_{\xi=\frac{x_4}{\lambda f_o},\quad \eta=\frac{y_4}{\lambda f_o}}, \tag{14}$$

where

$$W_1(x,y)=\frac{(f_\lambda-f_c)}{2f_c^2}(x^2+y^2). \tag{15}$$

Equation (14) indicates that the optical field across the plane x_4y_4 is the Fourier transform of a general pupil function, multiplied by two phase factors. The general pupil function is the physical exit pupil multiplied by a quadratic phase function $\exp[jkW_1(x,y)]$. This quadratic phase function can be considered as a wave aberration, which is due to defocusing when the operating wavelength is at λ other than the central wavelength λ_c. At λ_c, the quadratic phase factor disappears, and the spherical wavefront leaving the exit pupil is converging toward the focus in x_4y_4. However, at the operating wavelength λ, the spherical wavefront leaving the exit pupil is converging toward the focus in front of or behind x_4y_4. In this case, the distance Δz between the imaging plane and the observing plane is given by Eq. (4). If we treat the wavefront emitting from the exit pupil at λ_c as the reference sphere and define the wave aberration as the optical path length along a ray between the reference sphere and the actual wavefront, then the wave aberration can be approximated by

$$W(x,y)=\frac{\Delta z}{2d_i^2}(x^2+y^2), \tag{16}$$

where d_i is the distance between the exit pupil and the observation plane. In this case, $d_i=f_o$. Substituting Eq. (4) into Eq. (16), we can obtain the same result as Eq. (15). With this concept, we can greatly simplify the analysis of the point spread function of the second subsystem from plane x_4y_4 to plane x_5y_5.

If the reflection coefficient of the mirror at the plane x_4y_4 is R, the reflected optical field is then

$$U_4^+(x_4,y_4)=RU_4^-(x_4,y_4), \tag{17}$$

which is the input for the subsystem from plane x_4y_4 to plane x_5y_5.

The plane x_5y_5 is located at the focal plane of the diffractive lens at the central wavelength. So at λ_c, a point source at the plane x_4y_4 is imaged backward through the second subsystem to the plane x_5y_5, while at the other wavelength λ, a point source at the plane x_4y_4 is imaged to a plane in front of or behind the plane x_5y_5. If the observation plane is fixed at the plane x_5y_5 and we use the spherical wave converging toward this plane as a reference, the distance Δz between the observation plane and the image plane at λ is Δf, as given by Eq. (3). For this subsystem, the entrance pupil is the physical aperture of the objective lens, so the exit pupil $p_2(x,y)$ is its geometrical image through the diffractive lens. According to the Gaussian lens law, at λ_c the distance between the exit pupil and the observation plane x_5y_5 is

$$d_{i2}=\frac{f_c^2}{f_o}, \tag{18}$$

and if the size of the entrance pupil is a_1, the size of the exit pupil is found to be

$$a_2=a_1\frac{f_c}{f_o}. \tag{19}$$

Substituting Δf and Eq. (18) into Eq. (16), we obtain the wave aberration function

$$W_2(x,y)=\frac{\Delta f f_o^2}{2f_c^4}(x^2+y^2). \tag{20}$$

Then the general pupil function takes the form

$$p_2(x,y)\exp[jkW_2(x,y)]=p_2(x,y)\exp\left[jk\frac{f_o^2\Delta f}{2f_c^4}(x^2+y^2)\right], \tag{21}$$

and the point spread function of the second subsystem is given by

$$h_2(x_5,y_5)=U_5(x_5,y_5)$$
$$=CQ(x_5,y_5,d_{i2})F\left\{p_2(x,y)\exp\left[jk\frac{f_o^2\Delta f}{2f_c^4}\times(x^2+y^2)\right]\right\}\Bigg|_{\xi=\frac{x_5}{\lambda d_{i2}},\quad \eta=\frac{y_5}{\lambda d_{i2}}}. \tag{22}$$

Finally, the impulse response of the object arm is the ideal geometrical image of $U_4^+(x_4,y_4)$ at the plane x_5y_5 convoluted by the point spread function of the second subsystem, e.g., Eq. (22). Taking into account of the property of inverse imaging of the second subsystem, we can write the impulse response function as

$$h(x_5,y_5)=\frac{1}{M}U_4^+\left(-\frac{\tilde{x}}{M},\quad\frac{\tilde{y}}{M}\right)^{**}\times CQ(\tilde{x},\tilde{y},d_{i2})F\left\{p_2(x,y)\times\exp\left[jk\frac{f_o^2\Delta f}{2f_c^4}(x^2+y^2)\right]\right\}\Bigg|_{\xi=\frac{\tilde{x}}{\lambda d_{i2}},\quad\eta=\frac{\tilde{y}}{\lambda d_{i2}}},\tag{23}$$

where $U_4^+(-\tilde{x}/M,-\tilde{y}/M)$ is the ideal geometric image, and M is the magnification factor defined by $M=f_c/f_o$.

The impulse response of the reference arm can be analyzed similarly. In this arm, if the chromatic aberration can be neglected, when the operating wavelength is changed, the point source in the plane x_1y_1 can still be correctly imaged onto the reference mirror and then imaged back to the plane x_5y_5. Assume the focal length of the refractive lens L3 and the objective lens L4 are f_3 and f_o', respectively, $p_1'(x,y)$ is the aperture function of the objective lens L4, then the point spread function of the first subsystem (from plane x_1y_1 to $x_4'y_4'$) is expressed by

$$h_1'(x_4',y_4')=C'Q(x_4',y_4',f_o')F[p_1'(x,y)]\Big|_{\xi=\frac{x_4'}{\lambda f_o'},\quad\eta=\frac{y_4'}{\lambda f_o'}},\tag{24}$$

where $C'=B_{12}'B_{23}'B_{34}'B_\lambda'$, $B_\lambda'=j\lambda(f_3+f_o')$. The reflected optical field from the reflection mirror at plane $x_4'y_4'$ is

$$U_4^{+\prime}(x_4',y_4')=RU_4^{-\prime}(x_4',y_4')=Rh_1'(x_4',y_4').\tag{25}$$

For the second subsystem from plane $x_4'y_4'$ to plane x_5y_5, as in the object arm, the entrance pupil is the physical aperture of the objective lens, and the exit pupil $p_2'(x,y)$ is its geometrical image through the lens L3. The point spread function of the second subsystem takes the form

$$h_2'(x_5,y_5)=C'Q(x_5,y_5,d_{i2}')F[p_2'(x,y)]\Big|_{\xi=\frac{x_5}{\lambda d_{i2}'},\quad\eta=\frac{y_5}{\lambda d_{i2}'}},\tag{26}$$

where d_{i2}' is the distance between the exit pupil and plane x_5y_5, given by $d_{i2}'=f_3^2/f_o'$, a_2' is the size of the exit pupil of the second subsystem given by $a_2'=a_1'f_3/f_o'$ (a_1' is the size of the objective lens L4). Finally, the impulse response of the reference arm can be written as

$$h'(x_5,y_5)=\frac{1}{M'}U_4^{+\prime}\left(-\frac{\tilde{x}}{M'},\quad-\frac{\tilde{y}}{M'}\right)^{**}C'\times Q(\tilde{x},\tilde{y},d_{i2}')F[p_2'(x,y)]\Big|_{\xi=\frac{\tilde{x}}{\lambda d_{i2}'},\quad\eta=\frac{\tilde{y}}{\lambda d_{i2}'}},\tag{27}$$

where $U_4^{+\prime}(-\tilde{x}/M',-\tilde{y}/M')$ is the ideal geometric image and M' is the magnification factor of the second subsystem given by $M'=f_3/f_o$.

Based on this analysis, we can obtain the coherence function of the system versus wavelength for the two wavefields at x_5y_5, which are originated from the same point source at x_1y_1. When the two fields are overlapped, the resulting intensity consists of a bias term and a correlation term. Here we are only concerned with the correlation term. Generally speaking, the correlation signal is sinusoidal with a fairly constant frequency modulated by another envelope function. This envelope function represents the coherence between the two signals from the object and reference arms. Assume that the maximum optical path difference between the two waves is much smaller than the coherence length of the laser, the correlation function between the two waves can be represented by the mutual intensity, and the coherence degree factor can be expressed by the modus of the mutual intensity. Then at the ideal image position of the original point source, we have

$$\begin{aligned}\gamma(\lambda)&=|J|=|<h(x_5,y_5)h'^*(x_5,y_5)>|_{x_5=0,y_5=0}\\&=\Bigg|\Bigg\{\int\int C'Q(x_4',y_4',f_o')F[p_1'(x,y)]\Big|_{\xi=\frac{x_4'}{\lambda f_o'},\quad\eta=\frac{y_4'}{\lambda f_o'}}\\&\quad\times\delta\left(x_4'+\frac{\tilde{x}}{M'},y_4'+\frac{\tilde{y}}{M'}\right)C'Q(-\tilde{x},-\tilde{y},d_{i2}')\\&\quad\times F[p_2'(x,y)]\Big|_{\xi=\frac{-\tilde{x}}{\lambda d_{i2}'},\quad\eta=\frac{-\tilde{y}}{\lambda d_{i2}'}}d\tilde{x}d\tilde{y}\Bigg\}\\&\quad\times\Bigg\{\int\int\{CQ(x_4,y_4,f_o)F\{p(x,y)\\&\quad\times\exp[jkW_1(x,y)]\}\Big|_{\xi=\frac{x_4}{\lambda f_o},\quad\eta=\frac{y_4}{\lambda f_o}}\\&\quad\times\delta\left(x_4+\frac{\tilde{x}}{M},y_4+\frac{\tilde{y}}{M}\right)\\&\quad\times CQ(-\tilde{x},-\tilde{y},d_{i2})F\{p_2(x,y)\\&\quad\times\exp[jkW_2(x,y)]\}\Big|_{\xi=\frac{-\tilde{x}}{\lambda d_{i2}},\quad\eta=\frac{-\tilde{y}}{\lambda d_{i2}}}d\tilde{x}d\tilde{y}\Bigg\}\Bigg|.\end{aligned}\tag{28}$$

For an interference microscope, the depth discrimination is determined by the FWHM (full-width half-maximum) of

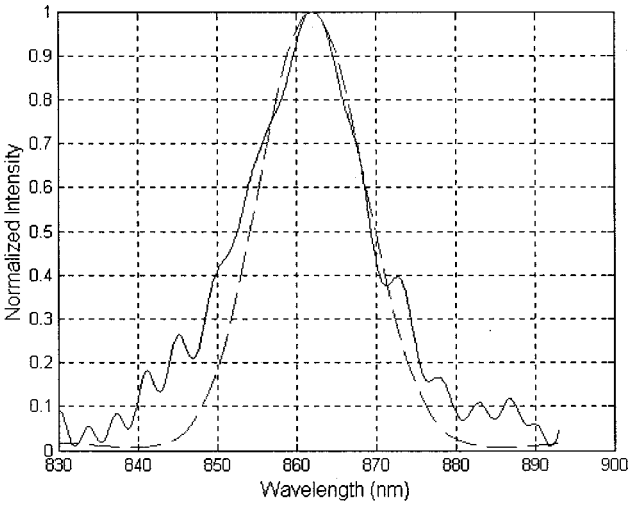

Fig. 2 Theoretical modeling of the correlation intensity envelope function of the system versus wavelength (dashed line). The solid line is the correlation intensity envelope function obtained with the experimental values described in the next section.

the correlation intensity envelope function, i.e., the squared amplitude envelope of γ. It is directly comparable to the output of a confocal microscope. As an example, we employ the parameters to be used in the experiment for simulation. Assume $f_3 = f_c = 125$ mm, $f_o = f_o' = 2.5$ mm, $a_1 = a_1' = 4.5$ mm, $\lambda c = 863$ nm, and $\Delta f/\Delta\lambda = 1.05 \times 10^5$. Figure 2 shows the theoretical normalized correlation intensity envelope function versus wavelength (dashed line). The FWHM is about 16.0 nm in wavelength, which corresponds to 0.68 μm in geometrical distance. It is seen that the maximum coherence degree factor occurs at the wavelength when the mirror is placed at the image plane of the point source. If the mirror is moved a little away, the maximum coherence factor will occur at the other wavelength. This achieves a wavelength-to-depth encoding. If the encoding is calibrated, this technique can be used to 3-D profilometry. Like the other interference microscopes, our system also has the same transverse resolution as the confocal microscope. The high lateral resolution results from reduced crosstalk between laterally adjacent cells. The correlation term will be zero unless the overlapped fields are from the same coherence pair.

If a 3-D object is placed around the focal plane of the objective lens at a fixed operating wavelength, all the object points exactly in the corresponding image plane of the source will be correctly imaged back to the plane x_5y_5. The optical fields from these points will interfere with the corresponding coherence cells from the reference arm with the maximum coherence degree factor and high-contrast fringes being formed at these points. The interference patterns are then imaged onto the CCD. Meanwhile, the optical waves illuminating all object points that are located at the other depth positions are defocused. When they are transmitted back to x_5y_5, the coherence degree factor between these fields and those from the reference mirror will decrease, resulting in lower contrast interference fringes or even no fringes on the CCD. On the other hand, for a fixed point on the object, when the wavelength is tuned over a range within which there is one certain wavelength corresponding to the axial position of this point, the output intensity can be recorded. As is described in the following section, the correlogram, obtained by removing the bias intensity, can be demodulated to find the peak amplitude of the envelope and the corresponding wavelength. According to the calibrated wavelength-to-depth coding, a 3-D image of the object can be obtained.

3 Experimental Results

The wavelength of the laser is tuned by an electronic step motor under microcomputer control and monitored via 50% beamsplitter BS1 using a wavemeter of the laser with a sensitivity of ± 0.02 nm. A power meter via beam splitter BS2 is used to monitor the power in real time. The laser beam is then introduced into a spatial filter and collimated. Both of the two 100× objective lens from Leitz Wetzlar have a numerical aperture (NA) of 0.9.

To calibrate the wavelength-to-depth encoding, we used a flat mirror as the object. This mirror is driven along the longitudinal axis by a piezoelectric transducer (PZT). In each step, the PZT moves 0.1 μm, and the whole measurement takes 64 steps. At a given wavelength, e.g., $\lambda_1 = 830$ nm, the interference fringes at one point (x,y) are recorded as the object mirror is scanned in the z direction. The fringes are demodulated to find the center of the mass of the envelope and the corresponding z-location $z_1(x,y)$. Demodulation can be done by the following steps:

1. Carry out the Fourier transform of all the intensity values recorded in each step. The result includes three separated parts: a package of positive frequency components, a package of negative frequency components, and the bias component.
2. Disregard the package of negative frequency components and the bias component, and use a high bandpass filter to choose the positive frequency components.
3. Center the package of positive frequency components and take the inverse Fourier transform to obtain the envelope function.

When the envelope function is obtained, a center-of-mass technique is used to determine the depth position. This location is the focal point position of the point (x,y) at λ_1. Then increase the wavelength to λ_2, repeat the operation, and get the z-location $z_2(x,y)$ of the focal point with the same transverse position at λ_2, and so on. In our case, the wavelength is tuned from 830 to 894 nm with an increment of 2 nm. Figure 3 is the calibration plot of the longitudinal focal position of one pixel with response to the wavelength (the depth position was measured from the right side of the object plane). By linear curve fitting the result, the slope of the curve is found to be 0.04216 μm/nm. Due to the aberrations existing in the imaging lenses, there may be very small variations among the slopes obtained at different pixels. By averaging the values of the slope for pixels in a certain area, the factor for wavelength-to-depth encoding was $\Delta z/\Delta\lambda = 0.04249$ μm/nm. According to Eq. (4), the sensitivity of the system depends on the

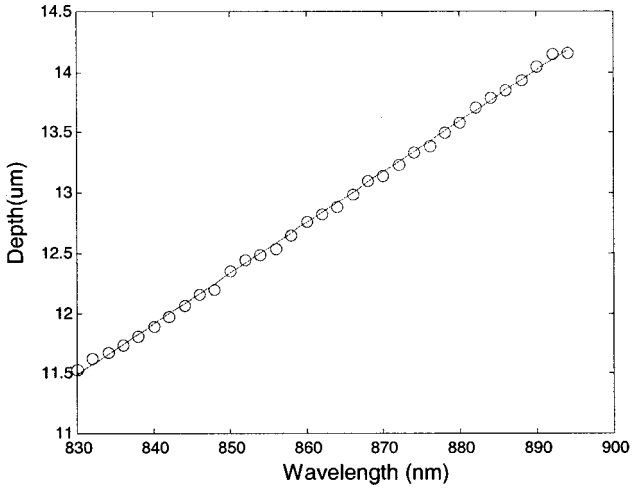

Fig. 3 Calibration for the wavelength-to-depth encoding.

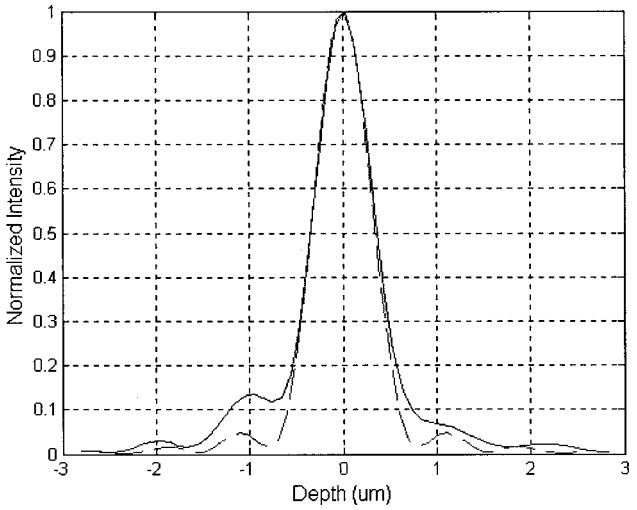

Fig. 4 Experimental depth-response envelope of the interference microscope with wavelength-to-depth scanning.

demagnification power $[(f_o/f_c)^2]$ of the 4-f imaging system and the dispersion strength $[f(\lambda_d)/\lambda_d]$ of the diffractive lens.

To measure the depth discrimination with the wavelength-to-depth encoding, we fixed the object mirror and tuned the wavelength from 830 to 893 nm with an interval of 0.25 nm. At each wavelength, the output power of the laser was monitored and the interference fringes were recorded. The intensity of the interference fringes was normalized according to the power of the laser and the spectral response of the CCD detector. The intensity values are demodulated in the same way as previously described. The normalized intensity envelope function is shown in Fig. 2 (solid line). The FWHM value is approximately 16.7 nm. According to the wavelength-to-depth calibration, this wavelength width corresponds to 0.71 μm in depth. The experimental result is basically consistent with the theoretical simulation.

For comparison, we also measured the depth discrimination capability of our system with mechanic scanning. To measure the depth response with mechanic scanning, we still put a flat mirror in the object plane. The movement of the object driven by the PZT is the same as that in the wavelength-to-depth calibration. The wavelength is tuned at 863 nm. The intensity patterns of one point (x,y) are recorded as the object mirror is moved in the vertical direction. The fringes are demodulated, as described before, to obtain the amplitude envelope function. The intensity envelope function is shown in Fig. 4, where the solid line is the experimental result and the dashed line is the theoretical value calculated in terms of Eq. (8) in Ref. 6. Both the experimental and the theoretical FWHM values are about 0.70 μm at 863 nm. It is seen that the experimental result is very consistent with the theoretical simulation on the main lobe. The deviation between the experimental and theoretical results at the outer sidelobes is probably due to the aberrations of our system. In comparison, it is seen that the depth discrimination ability of our system with wavelength-to-depth encoding is the same as that with mechanic scanning. Similar to the confocal imaging, the larger the NA of the objective lenses, the narrower the envelope.

Quantitative measurement of a four-level grating has been performed.[13] A comparison of profile measurements was made between a Dektak profilometer and an interference microscope with two types of scanning techniques. It is seen that the results obtained from the wavelength-to-depth encoding technique are comparable with those obtained from the other two techniques.

4 Conclusion

A new interference microscope based on a wavelength-to-depth encoding technique has been analyzed. It is shown that the experimental result of the depth resolution measurement is in good agreement with the theoretical analysis. The technique also offers comparable depth resolution as a traditional mechanical scanning technique. With the rapid development of wavelength-tunable lasers,[17] this technique is promising for fast, noncontact, and high-resolution 3-D imaging.

Acknowledgment

This work was supported by the National Science Foundation. Guoqiang Li is on leave from Shanghai Institute of Optics and Fine Mechanics, Academia Sinica, P.O. Box 800-211, Shanghai 201800, China.

References

1. *Confocal Microscopy*, T. Wilson, Ed., Academic Press, New York (1990).
2. S. Yin, G. Lu, J. Zhang, and F. T. S. Yu, "Kinoform-based Nipkow disk for a confocal microscope," *Appl. Opt.* **34**, 5695–5698 (1995).
3. M. Gu and C. J. R. Sheppard, "Three-dimensional transfer functions in 4Pi confocal microscopes," *J. Opt. Soc. Am. A* **11**, 1615–1627 (1994).
4. P. C. Lin, P. C. Sun, L. Zhu, and Y. Fainman, "Single-shot depth-section imaging through chromatic slit-scan confocal microscopy," *Appl. Opt.* **37**, 6764–6770 (1998).
5. M. Davidson, K. Kaufman, I. Mazor, and F. Cohen, "An application of interference microscopy to integrated circuit inspection and metrology," *Proc. SPIE* **775**, 233–247 (1987).
6. G. Kino and S. Chim, "Mirau correlation microscope," *Appl. Opt.* **29**, 3775–3783 (1990).
7. F. C. Chang and G. Kino, "325-nm interference microscope," *Appl. Opt.* **37**, 3471–3479 (1998).
8. B. S. Lee and T. Strand, "Profilometry with a coherence scanning microscope," *Appl. Opt.* **29**, 3784–3788 (1990).
9. T. Dresel, G. Hausler, and H. Venzke, "Three-dimensional sensing of rough surfaces by coherence radar," *Appl. Opt.* **31**, 919–925 (1992).

10. P. J. Caber, ''Interferometric profiler for rough surfaces,'' *Appl. Opt.* **32**, 3438–3441 (1993).
11. P. C. Sun and E. Arons, ''Nonscanning confocal ranging system,'' *Appl. Opt.* **34**, 1254–1261 (1995).
12. A. Dubois, A. C. Boccara, and M. Lebec, ''Real-time reflectivity and tomography imagery of depth-resolved microscopic surfaces,'' *Opt. Lett.* **24**, 309–311 (1999).
13. G. Li, P. C. Sun, P. C. Lin, and Y. Fainman, ''Interference microscopy for 3D imaging with a wavelength-to-depth encoding,'' *Opt. Lett.* **25**, 1505–1507 (2000).
14. L. Mandel and E. Wolf, *Optical Coherence and Quantum Optics*, Chap. 4 (Cambridge University Press, New York (1995).
15. S. Dobson, P. C. Sun, and Y. Fainman, ''Diffractive lenses for chromatic confocal imaging,'' *Appl. Opt.* **36**, 4744–4748 (1997).
16. J. W. Goodman, *Introduction to Fourier Optics*, Chaps. 5 and 6, McGraw-Hill, New York (1996).
17. F. Delorme, G. Alibert, C. Ougier, S. Slempkes, and H. Nakajima, ''Sampled-grating DBR lasers with 101 wavelengths over 44 nm and optimized power variation for WDM applications,'' *Electron. Lett.* **34**, 279–281 (1998).